Acta Oceanol. Sin., 2024, Vol. 43, No. 5, P. 133–144
https://doi.org/10.1007/s13131-024-2320-0
http://www.aosocean.com
E-mail: ocean2@hyxb.org.cn

An empirical method for joint inversion of wave and wind parameters based on SAR and wave spectrometer data

Yong Wan[1]*, Xiaona Zhang[1], Shuyan Lang[2, 3], Ennan Ma[4], Yongshou Dai[1]

[1] College of Oceanography and Space Informatics, China University of Petroleum, Qingdao 266580, China

[2] National Satellite Marine Application Center, Beijing 100081, China

[3] Key Laboratory of Space Ocean Remote Sensing and Application, Ministry of Natural Resources, Beijing 100081, China

[4] College of Control Science and Engineering, China University of Petroleum, Qingdao 266580, China

Received 9 October 2023; accepted 25 December 2023

Abstract

Synthetic aperture radar (SAR) and wave spectrometers, crucial in microwave remote sensing, play an essential role in monitoring sea surface wind and wave conditions. However, they face inherent limitations in observing sea surface phenomena. SAR systems, for instance, are hindered by an azimuth cut-off phenomenon in sea surface wind field observation. Wave spectrometers, while unaffected by the azimuth cutoff phenomenon, struggle with low azimuth resolution, impacting the capture of detailed wave and wind field data. This study utilizes SAR and surface wave investigation and monitoring (SWIM) data to initially extract key feature parameters, which are then prioritized using the extreme gradient boosting (XGBoost) algorithm. The research further addresses feature collinearity through a combined analysis of feature importance and correlation, leading to the development of an inversion model for wave and wind parameters based on XGBoost. A comparative analysis of this model with ERA5 reanalysis and buoy data for of significant wave height, mean wave period, wind direction, and wind speed reveals root mean square errors of 0.212 m, 0.525 s, 27.446°, and 1.092 m/s, compared to 0.314 m, 0.888 s, 27.698°, and 1.315 m/s from buoy data, respectively. These results demonstrate the model's effective retrieval of wave and wind parameters. Finally, the model, incorporating altimeter and scatterometer data, is evaluated against SAR/SWIM single and dual payload inversion methods across different wind speeds. This comparison highlights the model's superior inversion accuracy over other methods.

Key words: synthetic aperture radar (SAR), wave spectrometer, extreme gradient boosting (XGBoost), joint inversion method, wave and wind parameters

Citation: Wan Yong, Zhang Xiaona, Lang Shuyan, Ma Ennan, Dai Yongshou. 2024. An empirical method for joint inversion of wave and wind parameters based on SAR and wave spectrometer data. Acta Oceanologica Sinica, 43(5): 133–144, doi: 10.1007/s13131-024-2320-0

1 Introduction

The ocean, abundant in resources like surface wind fields and waves, presents significant research opportunities. Sea surface wind fields, a primary driver of ocean surface dynamics, and sea waves, a dynamic phenomenon influenced by these winds and other factors, are intricately linked. Studying and monitoring these elements is vital for national defense, maritime navigation, and marine resource exploitation (Zou et al., 2018; Huang et al., 2021).

The advancement of satellite technologies, including synthetic aperture radar (SAR) and wave spectrometers, has introduced novel approaches for the observation of wind fields and waves. SAR, as an active microwave sensor, offers high-resolution wave mode data, enabling all-day and all-weather sea detection.

Nonetheless, SAR is subject to the impact of factors like the radial component of peak phase velocity, resulting in the occurrence of high azimuth wave-number cut-off (Alpers and Bruening, 1986; Li et al., 2002). In practical terms, this means that waves smaller than the cut-off wavelength manifest in SAR images as various other parameters and image noise, including but not limited to variance and kurtosis.

Furthermore, within the context of SAR wind field inversion, a majority of methods necessitate the inclusion of external wind direction data as input, rendering it incapable of independently acquiring wind information. The wave spectrometer is an innovative form of active microwave remote sensing radar. It operates by capturing the backscattering coefficient of the sea surface at small incidence angles ranging from 0° to 10°. Subsequently, it extracts the wave spectrum along with various integral wave parameters, all without encountering the issue of high wave number cut-off in the azimuth direction. Moreover, the wave spectrometer has the capability to deduce wind direction based on the connection between radar azimuth and backscattering coefficient. However, it's important to note that the data resolution of surface wave investigation and monitoring (SWIM) stands at 70 km × 90 km, a considerable difference from the higher resolution of SAR wave mode, which is approximately 5 m × 5 m (Han et al., 2013). Considering the features of both SAR and the wave

---

Foundation item: The project supported by Key Laboratory of Space Ocean Remote Sensing and Application, Ministry of Natural Resources under contract No. 2023CFO016; the National Natural Science Foundation of China under contract No. 61931025; the Innovation Fund Project for Graduate Student of China University of Petroleum (East China); the Fundamental Research Funds for the Central Universities under contract No. 23CX04042A.

*Corresponding author, E-mail: wanyong@upc.edu.cn

spectrometer, it becomes evident that the wave spectrometer can furnish preliminary wind direction data for SAR wind field parameter inversion. Furthermore, it can compensate for SAR's azimuth cut-off effect, thereby enhancing the precision of integral wave parameter inversion. Hence, the approach of integrating SAR and the wave spectrometer for wave and wind parameter inversion holds promise as an ideal method for extensive and enduring marine environment monitoring in the future. It presents a fresh perspective for the future of ocean observation.

After years of development, both domestic and international researchers have put forward various methods for wave and wind parameter inversion, leveraging SAR and wave spectrometers. Concerning the integration of ocean wave parameter inversion, SAR primarily employs two categories of methods. The first category relies on mathematical statistics and includes notable approaches such as the Max Planck Institute (MPI) method (Hasselmann and Hasselmann, 1991), the semi-parametric retrieval algorithm (SPRA) (Hasselmann and Hasselmann, 1991), the parameterized first-guess spectrum method (PFSM) (Mastenbroek and De Valk, 2000; He, 1999), and the partition rescaling and shift algorithm (PARSA) (Schulz-Stellenfleth et al., 2005).

While the aforementioned methods have demonstrated the capability to effectively extract wave spectra from SAR image spectra, their inversion accuracy heavily relies on prior information, and the conversion relationship between the SAR image spectrum and wave spectrum is intricate. Consequently, researchers have subsequently introduced an alternative category of empirical methods for integral wave parameter inversion (Huang et al., 2017). This primarily encompasses the CWAVEs algorithms (including CWAVE_ERS (Schulz-Stellenfleth et al., 2006), CWAVE_ENV (Li et al., 2011), CWAVE_S1A (Stopa and Mouche, 2017), and CWAVE_EX (Pleskachevsky et al., 2022)) designed for C-band SAR, as well as the XWAVE, XWAVE-2, and XWAVE-C algorithms for X-band SAR (Bruck and Lehner, 2013, 2015; Pleskachevsky et al., 2016). However, it's noteworthy that the majority of the aforementioned empirical methods for C-band radar predominantly focus on the inversion of either significant wave height or wind speed under specific SAR observation modes. Simultaneously achieving high-precision inversion for both significant wave height and wind speed remains a challenge.

The viability of wave spectrum measurement using a wave spectrometer has also been substantiated. Researchers have sequentially undertaken pertinent investigations, including ROWS, RESSAC, and STORM (Jackson, 1987; Hauser et al., 1992), and their findings indicate that the wave spectrometer can effectively measure wave spectrum information with wavelengths exceeding 70 m. This implies that integral wave parameter inversion with the wave spectrometer remains unaffected by azimuth cut-off limitations (Hauser et al., 2001). Regarding the acquisition of wind parameters, researchers commonly employ Geophysical Model Functions (GMF) when utilizing SAR for wind information retrieval. This method is an empirical model built upon certain SAR parameters and statistical wind speed data. Currently, the GMFs predominantly applicable to C-band SAR encompass CMOD4 (Stoffelen and Anderson, 1997), CMOD-IFR2 (Quilfen et al., 1998), CMOD5 (Hersbach et al., 2007), and COMD5.N (Hersbach, 2010). Furthermore, Wang (2016) conducted a discussion on the notable anisotropy of the sea surface backscattering coefficient when utilizing wave spectrometer data within the incidence angle range of 4° to 18° . Li (2019) conducted a study on the anisotropy and asymmetry of radar backscatter coefficients under low incident angles in rain-free conditions. The study's findings concluded that wind speed and wind direction parameters were well-suited for SWIM inversion. Ren et al. (2016) posited that SAR and the Wave Spectrometer represent two complementary microwave sensors and introduced an inversion approach for wave spectrum using SAR and SWIM data. Building upon this, Wan et al. (2022) devised a mechanism-driven method for the concurrent inversion of wave and wind parameters through the collaboration of SAR and the Wave Spectrometer. Nevertheless, it's worth noting that the mechanism-based method proposed in the literature still relies on prior information.

We propose an empirical method for the simultaneous inversion of wave and wind parameters using SAR and Wave Spectrometer data. Section 2 outlines the data sets and model-building approaches employed in this study. In Section 3, we assess and discuss the significance and relevance of the feature parameters, providing guidance for model parameter selection. Section 4 establishes the inversion model, and we compare its output with wave and wind parameters obtained from the European Centre for Medium-Range Weather Forecasts (ECMWF) and the National Data Buoy Center (NDBC) buoy data. Furthermore, we engage in a comparative analysis and discussion of the model output with inversion results derived from a single payload. Section 5 concludes our study.

2 Materials

This study primarily relies on SAR wave mode data, wave spectrometer data, ECMWF ERA5 data, NDBC buoy data, scatterometer data, and altimeter data. Additionally, we employ the extreme gradient boosting (XGBoost) algorithm for our modeling efforts, which will be elaborated upon in subsequent sections.

2.1 *Sentinel-1 data*

The Sentinel-1 mission comprises two satellites, namely, Sentinel-1A and Sentinel-1B. European Space Agency (ESA) launched Sentinel-1A on April 3, 2014, with a revisit period of 12 d. Subsequently, with the launch of Sentinel-1B on April 26, 2016, these two satellites have been capable of collaborating in Earth observation efforts. The satellite's revisit period has been shortened to 6 d. Sentinel-1 SAR offers four distinct imaging modes: interferometric wide swath (IW), stripmap (SM),extra wide swath (EW), and wave mode (WV). In this study, we utilized the VV-polarized WV mode data from Sentinel-1 in single-look complex (SLC) format to investigate the sea wave wind field characteristics within our designated study area. The WV mode serves as the default imaging mode employed by SAR satellites for sea surface observation. SAR images were acquired alternatively along the orbit at incidence angles approximately measuring 23° (WV_1) and 36° (WV_2). In this paper, the radar data utilized corresponds to incidence angles ranging from approximately 22.7332° to 24.2977° for WV_1 and from approximately 35.9855° to 37.3127° for WV_2. The data resolution is specified as 2.0 m × 4.8 m for WV_1 and 3.1 m × 4.8 m for WV_2 (Pleskachevsky et al., 2022).

2.2 *CFOSAT SWIM data*

The China-France Oceanographic Satellite (CFOSAT), a collaborative maritime satellite project between China and France, features two payloads: a scatterometer developed by China and a wave spectrometer developed by France. Launched from Jiuquan on October 29, 2018, CFOSAT features the groundbreaking SWIM, the world's first space-borne spectrometer. SWIM operates within the Ku band and serves as a wave information detection radar, uniting an altimeter with a small incidence angle multi-beam true aperture imaging radar. This integration enables it to conduct all-day, near-all-weather sea detection, with the capability of utilizing multiple beams at angles of 0°, 2°, 4°, 6°, 8°, and 10° for enhanced performance. When the nadir point is at the 0° beam, the spectrometer functions as an altimeter to gauge the significant wave height, while the other beams are utilized to capture wave direction spectrum information.

In SWIM products, data from both land and sea are co-present. Therefore, the initial step in extracting geophysical parameters involves the removal of land-related data. Additionally, rainfall impacts the Normalized Radar Cross Section (NRCS) of the sea surface, subsequently affecting the retrieval of geophysical parameters. In this study, the flag provided in the product was employed to eliminate anomalous data associated with rain, land, and sea ice (Ren et al., 2021). Given the utilization of co-located SAR and SWIM data in this research, the SAR data underwent preprocessing in conjunction with the SWIM data.

When gathering collocated SAR/SWIM data, we utilize the central longitude and latitude of the SAR image to establish the spatial location for the SAR sub-image. To illustrate, for a SAR revisit period (December 1, 2019, to December 6, 2019), the distribution of collocated data locations is described (Fig. 1), with each point representing a set of collocated data. The color of each point corresponds to the numerical value of the significant wave height.

2.3 *ECMWF ERA5 data*

ECMWF has been providing global wind fields and wave data at various resolutions since 1979. In this study, we primarily rely on ECMWF ERA5 data, specifically the 10 m wind speed, 10 m wind direction, significant wave height, and mean wave period, encompassing both wind-generated and swell waves. These data are available at a resolution of 0.125°. To align the SAR data both temporally and spatially with ERA5 data, we employ the bilinear interpolation algorithm, ultimately obtaining ERA5 data that are collocated with SAR data in both time and space.

As the collocated data from the aforementioned three data sources were relatively limited, we acquired collocated data by comparing ERA5 data with buoy data. Figure 2 displays a scatter plot depicting the parameter comparisons between ERA5 and buoy data. Standard error metrics like root mean square errors

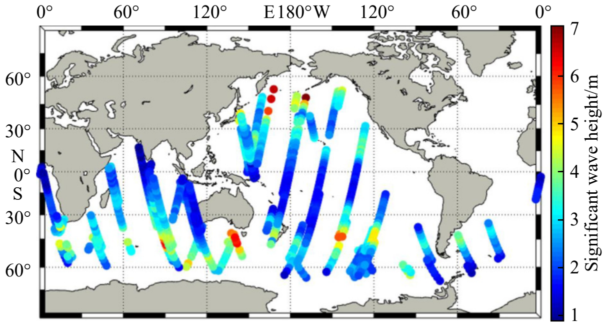

Fig. 1. Collocated data of SAR and SWIM (space window: 100 km, time window: 1.5 h) within a SAR revisit period (6 d).

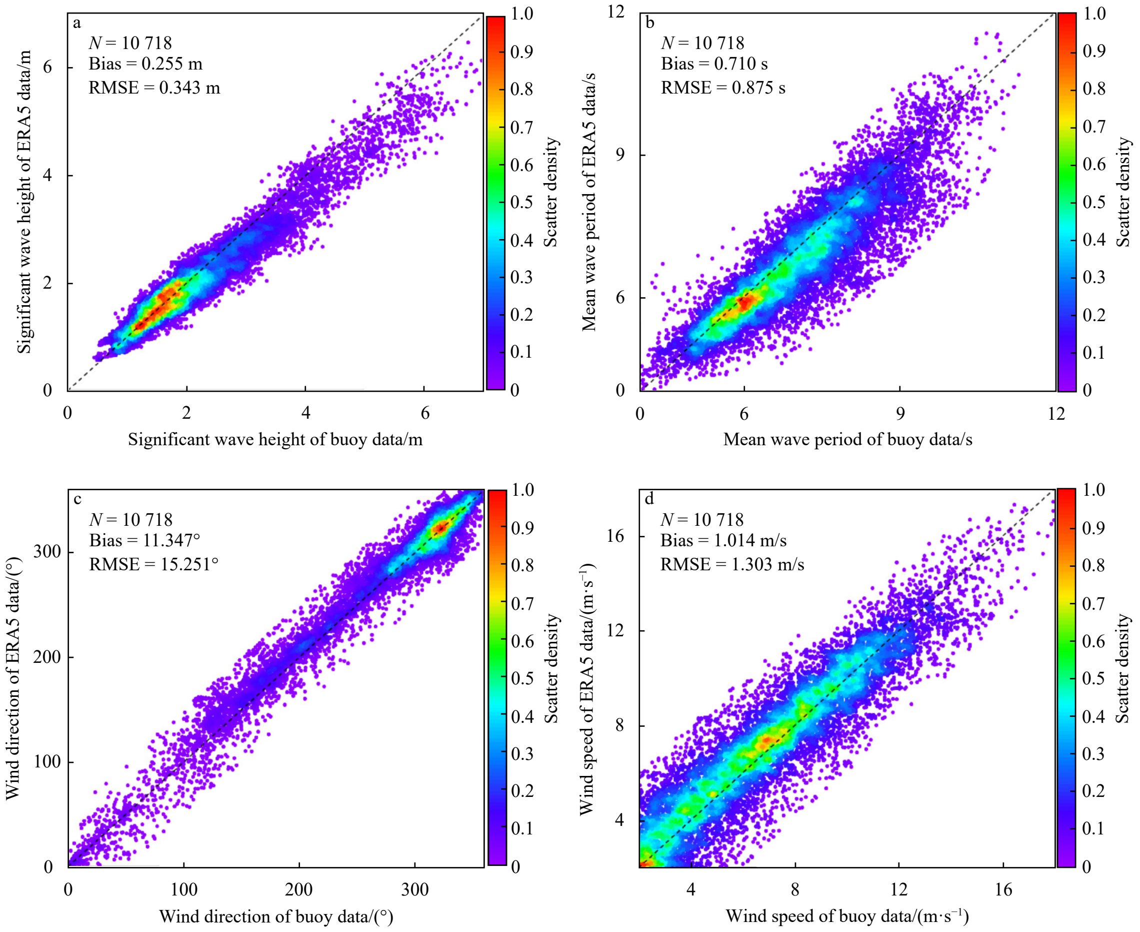

Fig. 2. Comparison of wave and wind parameters between ERA5 data and buoy data. a. Significant wave height, b. mean wave period, c. wind direction, and d. wind speed.

(RMSE) and bias are utilized to assess the accuracy of these comparisons. It is evident that the RMSE values for wind direction, wind speed, significant wave height, and mean wave period between ERA5 data and buoy data are 15.251°, 1.303 m/s, 0.343 m, and 0.875 s, respectively (Figs 2a, b, c, and d). This demonstrates a high level of agreement between the meteorological parameters provided by ERA5 data and buoy data. Consequently, we have chosen to utilize ERA5 data as the ground truth for assessing the accuracy of the established model for wave and wind parameter inversion.

2.4 *Buoy data*

Marine buoys represent the primary means for monitoring and predicting marine disasters globally. Presently, many countries have made significant advancements in marine buoy technology, approaching a state of refinement. Consequently, this study aims to utilize wind and wave data furnished by the NDBC as the ground truth for evaluating the accuracy of the empirical method employed to derive wave and wind parameters in this research. This paper demonstrates the alignment of the SAR images, the SWIM, and the buoy data (Fig. 3).

Given that the NDBC buoy offers wind speed data at 5 m above the sea surface, this study employs the wind speed at 10 m above the sea surface, necessitating the conversion of the provided NDBC buoy wind speed. The conversion formula utilized is as follows (Shao et al., 2017):

$$U_z = U_{z_m} \ln\left(z/z_0\right)/\ln\left(z_m/z_0\right), \qquad (1)$$

where U_z represents the wind speed (to be extrapolated) at height z; U_{z_m} is the known wind speed at height of z_m; z_0 is the length of the rough surface.

2.5 *CFOSAT scatterometer (SCAT) data*

The scatterometer onboard CFOSAT utilizes the Ku band at 13.256 GHz and features a dual-polarized antenna, offering a 360° observation azimuth (Lin and Dong, 2011). The echoes received by CSCAT share the same polarization as the transmitted pulse, resulting in both VV and HH polarization modes. In contrast to previous fixed sector beam scatterometers like Advanced Scatterometer (ASCAT), CFOSAT Scatterometer (CSCAT) exhibits no blind areas beneath the nadir point. Furthermore, when compared to the pencil scatterometer (Sea Winds), each wind vector unit of CSCAT provides a greater number of observations across various azimuths and incident angles (Spencer et al., 1997).

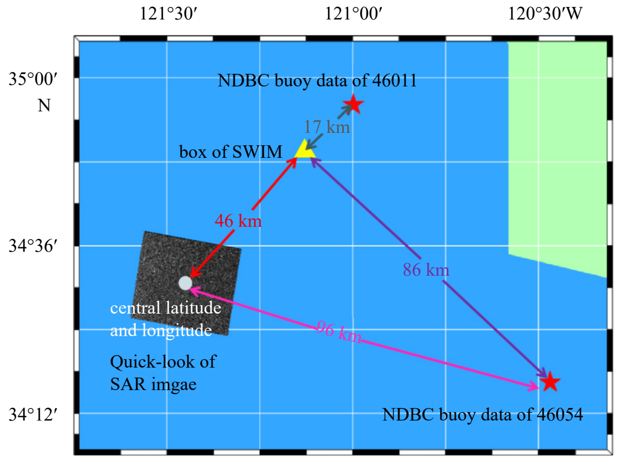

Fig. 3. Collocated data from SAR, SWIM, and NDBC buoys. The black square denotes the quick-look of the Sentinel-1B WV mode SAR image, acquired at 14:16 on September 11, 2019; the red stars and yellow triangles represent the positions of SAR-matched Buoys 46011, 46054, and SWIM.

The L2B product from CSCAT employed in this study offers a resolution of 25 km × 25 km. Derived from the L2A (Level 2A) data, the L2B (Level 2B) dataset is generated through processes like wind field inversion, ambiguity solution removal, and quality control, employing the geophysical model function NSCAT-4. This dataset primarily includes parameters such as wind speed, wind direction, background wind field, and other relevant information. For our verification purposes, we primarily utilize the wind speed data from this source as the ground truth to assess the accuracy of wind field information inversion in this research.

2.6 *Altimeter data*

In this study, Level 2 orbit data from Haiyang-2B (HY-2B), Haiyang-2C (HY-2C), and Sentinel-3A radar altimeters are utilized, with the significant wave height data from these satellite products serving as validation data for the research findings. Interested users can access HY-2B/C data via the Chinese marine satellite data service system at the following address: https://osdds.nsoas.org.cn/. Additionally, Sentinel-3A data can be downloaded through Copernicus Online Data Access from the following website: https://scihub.copernicus.eu/dhus/#/home.

2.7 *XGBoost*

In recent years, the XGBoost algorithm (Chen and Guestrin, 2016), emerging as a novel deep machine learning optimization technique, exhibits adaptability to intricate nonlinear relationships. Unlike traditional gradient boosting algorithms, XGBoost has undergone enhancements such as the incorporation of second-order Taylor expansion for the loss function, parallel feature splitting, and the introduction of regularization terms, among others. In contrast to other gradient boosting ensemble algorithms, XGBoost demonstrates superior speed and accuracy. Moreover, the model exhibits robust parallel processing capabilities, effectively addressing overfitting issues encountered in machine learning regression models. Hence, we employ this approach for the inversion of integrated sea state parameters and wind field parameters. XGBoost comprises multiple decision trees. Its fundamental concept involves amalgamating multiple tree models through iterative refinement, ultimately yielding a more accurate model. The subsequent explanation will delineate the implementation principles of XGBoost, focusing on the classification and regression tree (CART) and objective functions.

(1) CART

XGBoost is constructed by incorporating multiple CARTs to facilitate the integrated learning of multiple CART trees (Liu et al., 2021). Within the decision tree framework, each newly introduced tree is trained based on an already-trained tree. CART is a commonly employed technique in data processing. It encompasses two primary tree types: classification trees and regression trees. Given that this section focuses on utilizing a regression tree for research, we will use a regression tree as an illustrative example to delve into its generation process.

The approach employed by the CART algorithm to construct a regression tree is rooted in minimizing the square error. The square error is defined as follows:

$$L=\sum_{x_i}\left(y_i-f(x_i)\right)^2, \tag{2}$$

where y_i represents the true value, and $f(x_i)$ is the predicted value of the sample .

During the process of feature selection in the regression tree, the sum of square errors for all features and potential splitting points is computed individually. The feature and splitting point combination that results in the least sum of square errors is then selected as the optimal choice.

(2) Objective function

The primary objective of the XGBoost algorithm is to formulate a multi-objective optimization function with the highest degree of generalization. To enhance the model's classification performance, it is imperative to minimize the objective function, which is defined as follows (Chen and Guestrin, 2016):

$$O_{\mathrm{bj}}=\sum_{i=1}^{n} l\left(y_i,\hat{y}_i\right)+\sum_{k=1}^{K}\Omega\left(f_k\right), \tag{3}$$

where $\hat{y}_i$ is the prediction result for sample, f_k represents the k-th tree, i represents i-th sample in the data set, n is the total amount of data imported into the k-th class tree, l is the objective function after iteration, $\Omega(f_k)$ is an iterative model penalty term that can reduce model overfitting, and K represents all the established trees. The first term in the formula represents the traditional loss function, whose function is to measure the fitting degree of the model to the training data. The second term represents the regularization term, which is used to control the complexity of the model to prevent the overfitting phenomenon of the model. The smaller the value of this function, the lower the complexity and the stronger the generalization ability.

Referring to the idea of logistic regression iteration, when adding the t-th tree into the model, it can be expressed as

$$\hat{y}_i^{(t)}=\sum_{k=1}^{t} f_k(x_i)=\hat{y}_i^{k-1}+f_t(x_i), \tag{4}$$

where $\hat{y}_i^{k-1}$ is the prediction result of the first $k-1$ tree for sample x_i; f_t represents the t-th tree .

Taylor expansion method is adopted to approximate the original objective function and optimize the objective quickly. For the specific derivation process, see literature (Chen and Guestrin, 2016), i.e.,

$$O_{\mathrm{bj}}^{(t)}=\sum_{i=1}^{T}\left[g_i f_t\left(x_i\right)+\frac{1}{2}h_i f_t^2\left(x_i\right)\right]+\Omega\left(f_t\right), \tag{5}$$

where g_i and h_i are the first and second partial derivatives of the loss function, respectively. Each leaf node is split into a sample set and expanded as follows:

$$O_{\mathrm{bj}}^{(t)}=\sum_{j=1}^{T}\left[\left(\sum_{i\in I_j} g_i\right)\omega_j+\frac{1}{2}\left(\sum_{i\in I_j} h_i+\lambda\right)\omega_j^2\right]+\gamma T, \tag{6}$$

where $I_j=\{i\,|\,q(x_i)=j\}$, represents the leaf node j of the decision tree; ω_j represents the weight of leaf node j; λ and γ are the weighting factors; T is the number of leaf nodes.

If a fixed tree structure is selected, then the objective function is only related to leaf weight ω_j. By taking the derivative of the objective function concerning and substituting it into the objective function, the optimal solution can be obtained as

$$O_{\mathrm{bj}}^{(t)}=-\frac{1}{2}\sum_{j=1}^{T}\frac{\left(\sum_{i\in I_j} g_i\right)^2}{\sum_{i\in I_j} h_i+\lambda}+\gamma T. \tag{7}$$

3 Feature selection and model establishment

We propose an empirical method for the joint inversion of wave and wind parameters based on SAR and wave spectrometer data. Initially, feature parameters related to wave and wind parameters are extracted from SAR and SWIM data. Subsequently, the input feature parameters are ranked based on significant wave height, mean wave period, wind direction, and wind speed. Next, we calculate the Pearson correlation coefficient between each feature parameter. When a substantial correlation exists between two features, we remove the feature parameter with the lowest importance ranking to mitigate collinearity effects. Finally, we establish various inversion models using the XGBoost algorithm to obtain the wave and wind parameters. The inversion process is depicted (Fig. 4).

3.1 *Feature selection*

The selection of feature parameters constitutes the fundamental and pivotal aspect in the machine learning model construction process, with direct implications for both model efficiency and inversion outcomes. The subsequent section outlines

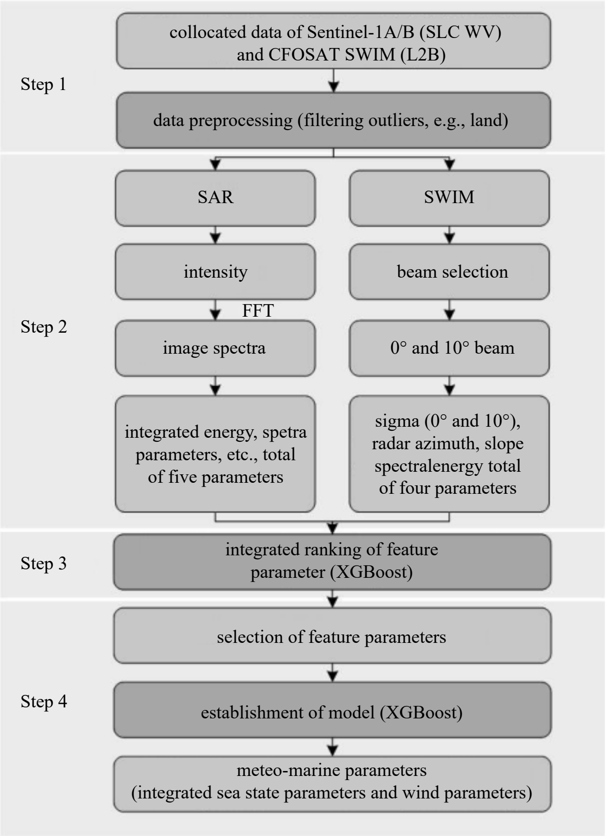

Fig. 4. The flow chart of the XGBoost regression. FFT, fast Fourier transform.

the feature parameter selection process based on SAR and SWIM data.

This paper initially addresses parameters associated with wave and wind within SAR data: (1) During SAR imaging of waves, the scattering plane element undergoes an azimuthal shift, rendering waves with wavelengths smaller than a specific threshold undetectable in SAR images. This phenomenon is termed azimuth cut-off. The cut-off wavelength constitutes a pivotal factor influencing the complete wave information in SAR observations and exhibits a strong correlation with wave parameters. Precisely determining the cut-off wavelength holds significant importance for comprehending the impact of cut-off wavelength on SAR wave observations. (2) SAR image backscattering coefficient and normalized variance have found extensive utility in extracting sea surface wind and wave parameters from SAR images. Furthermore, it has been substantiated that they exhibit a positive correlation with the significant wave height of sea waves (Wang et al., 2022). (3) The SAR wind speed inversion method, CMOD5.N, illustrates a discernible correlation between satellite incidence angle and backscattering coefficient with wind speed. (4) In alignment with the SAR wave spectrum inversion method, a robust correlation exists between the SAR image spectrum and the inverted wave spectrum. Consequently, this paper calculates and selects the SAR image spectral energy as a featured parameter.

Secondly, this paper considers parameters related to wave and wind within SWIM data: (1) With increasing incidence angle, the anisotropy of the backscattering coefficient becomes more pronounced, and a specific relationship exists between radar azimuth and downwind direction. Consequently, the feature parameters selected encompass the backscattering coefficient, radar azimuth, and the fuzzy value of radar azimuth at a 10° incidence angle. (2) In accordance with prior research (Li, 2019), the backscattering coefficient at the nadir point exhibits correlation with wind speed. (3) Furthermore, in reference (Wan et al., 2022), integrated wave parameters were derived through the combined utilization of SAR and wave spectrometer data. The slope spectrum of SWIM serves as the initial guess spectrum for the Max Planck Institute method, enabling the retrieval of integral wave parameters.

In summary, the input parameters chosen for the model inversion of wave and wind parameters encompass SAR's incidence angle, backscattering coefficient, normalized variance, image spectral energy, cut-off wavelength, and SWIM's backscattering coefficient at the nadir point, backscattering coefficient at a 10° incidence angle, radar azimuth, and slope spectral energy. The subsequent section provides a concise introduction to these feature parameters.

(1) Normalized image variance

$c_{\rm var}$ can be calculated from the average intensity of the image $\langle I\rangle$ (Schulz-Stellenfleth et al, 2006), as shown in Eq. (8):

$$c_{\rm var}={\rm var}\left(\left(I-\langle I\rangle\right)/\left\langle I\right\rangle\right). \tag{8}$$

(2) Azimuth cut-off wavelength

The cut-off wavelength demonstrates a robust correlation with integrated wave parameters (Liu et al., 2021), underscoring its pivotal role in understanding the impact of cut-off wavelength on SAR wave observations. Kerbaol et al. introduced a method in 1998 to estimate the cut-off wavelength by fitting the Autocorrelation Function (ACF) of SAR images (Wang et al., 2022). This technique is employed to determine the cut-off wavelength value. Initially, it performs Fourier transformation on the real part of the cross-spectrum of the SAR image to derive the autocorrelation function of the SAR image. Subsequently, it fits the autocorrelation function along the azimuthal direction with a Gaussian function, thus obtaining the cut-off wavelength.

A SAR image, being a single-look complex image, can be divided into two or more sub-looks through the application of a split-look processing technique. To derive the cross-spectrum between any two sub-looks, the Fourier transform of the correlation function is utilized. The split-look processing technique involves the generation of an azimuthal spectrum by performing fast Fourier transform (FFT) on a single-look image in the azimuthal direction. Following this, the three sub-views are separated using a Hamming window with the same frequency interval on the azimuthal spectrum. Inverse fast Fourier transform (IFFT) is performed on the azimuthal spectra of different sub-looks to obtain the intensity images of the corresponding sub-looks. The SAR image cross-spectrum can be obtained by performing cross-spectrum estimation on the intensity images of any two of these sub-looks. The image cross-spectrum $P^{1,\,2}$ of sub-looks m_1 and m_2 is defined as shown in Eq. (9):

$$P^{1,\,2}=\hat{m}_1(\hat{m}_2)^*, \tag{9}$$

where $\hat{m}_j\,(j=1,2)$ is the two-dimensional Fourier transform of $m_j\,(j=1,2)$ and $(m_j)^*$ is the complex conjugate of m_j.

The autocorrelation function of the SAR image is obtained by performing Fourier transform on the real part of the cross-spectrum. The azimuthally cut-off wave number can be obtained by fitting an autocorrelation function along the azimuthal direction using a Gaussian function $C(x)$ (Pleskachevsky et al., 2019), and the expression for the Gaussian function is shown in Eq. (10).

$$C(k_x;\,K_{\rm c})=\exp\left[-\pi\left(\frac{k_x}{K_{\rm c}}\right)^2\right], \tag{10}$$

where k_x represents the azimuthal wave number distance and $K_{\rm c}$ represents the cut-off wave number.

The relationship between the cut-off wavelength and cut-off wave number is illustrated in Eq. (11), providing a means to determine the cut-off wavelength.

$$\lambda_{\rm c}=\frac{2\pi}{K_{\rm c}}, \tag{11}$$

(3) Image spectral energy

To obtain the integral wave parameters, the FFT operation was applied to a sub-scene of the radiometric calibration. The image power spectrum ISP $\left(k_x,k_y\right)$ is calculated by integration in the two-dimensional wave number domain (Pleskachevsky et al., 2022; Kerbaol et al., 1996; Rikka et al., 2018).

$$E_{\rm ISP}=\int_{k_x^{\min}}^{k_x^{\max}}\int_{k_y^{\min}}^{k_y^{\max}}{\rm ISP}\left(k_x,k_y\right){\rm d}k_y{\rm d}k_x, \tag{12}$$

where $k_x^{\max}=k_x^{\min}=2\pi/L_{\min}\,({\rm rad/m})$ and $L_{\min}$ is the pixel spacing of the sub-scene. $k_y^{\max}=k_y^{\min}=2\pi/L_{\max}\,({\rm rad/m})$, and $L_{\max}$ is the sub-scene size (equal sub-scene resolution in the x and y directions).

(4) Slope spectrum energy

The slope spectrum $S(k,\theta)$ provided by SWIM Level 2 products can reflect the changing patterns of sea surface wind and waves, and the slope spectrum energy is defined as shown in

Eq. (13) (Pleskachevsky et al., 2019).

$$E_{\text{swim\_slope}} = \int_0^{2\pi} \int_{k_{\min}}^{k_{\max}} S(k, \theta)\, \mathrm{d}k\mathrm{d}\theta, \tag{13}$$

where $k_{\max}$ and $k_{\min}$ are the maximum and minimum wave numbers of each box of SWIM, respectively.

To establish a model for the accurate inversion of ocean wave and wind parameters, it is crucial to evaluate the correlation between input and output parameters. Therefore, in this section, the feature importance ranking function of XGBoost is employed to rank the importance of ten features extracted from SAR and wave spectrometer data. The output parameters consist of significant wave height (SWH), mean wave period (MWP), wind direction (WD), and wind speed (WS) provided by ERA5 data. The input parameters are derived from SAR and SWIM data. Additionally, Pearson correlation coefficients between pairs of feature parameters are calculated, and when these coefficients are high, the least important parameters are eliminated.

3.1.1 *Importance analysis*

The feature importance ranking module of the XGBoost algorithm is utilized to sort and screen features. This process involves counting the number of times each feature splits (with features that continue to bring gains to the model splitting more frequently, resulting in higher gain values). The final score value of each feature, based on the number of splits, serves as the basis for feature ranking. Subsequently, the hyperparameters of the XGBoost model are determined by minimizing the root mean square errors of SWH, MWP, WS, and WD obtained from the joint inversion of SAR and wave spectrometer data and the relevant parameters provided by ERA5. The optimal hyperparameters for XGBoost in this paper are detailed (Table 1).

Table 1. Optimal hyperparameter for XGBoost in this paper

Hyperparameter	Value
number of estimators	60
max_depth	20
learning_rate	0.1
reg_lambda	1
reg_alpha	0
min_child_weight	1

The importance evaluation scores of each feature parameter are depicted in Fig. 5. In Fig. 5a, the ordinate corresponds, from bottom to top, with SAR feature parameters: incident angle (θ), backscattering coefficient (sigma), normalized variance (c_{var}), image spectral energy (E_{s}), and cut-off wavelength (λ_{c}). And SWIM parameters: backscattering coefficient under nadir point (sigma 0°), backscattering coefficient at 10° incident angle (sigma 10°), slope spectral energy ($E_{\text{s\_slope}}$), radar azimuth 1 (φ_{radar1}, corresponding angle when the 10° backscattering coefficient is maximum) and ambiguity value of radar azimuth 1 (φ_{radar2}).

SAR incident angle, SWIM backscattering coefficient under the nadir point, SWIM slope spectral energy, and SAR normalized variance have the greatest influence on WD, WS, SWH, and MWP, respectively, which is consistent with the conclusions drawn by previous researchers (Fig. 5a). Next, by adding the importance evaluation scores of each feature parameter to the four output parameters, we obtained the total importance score of each feature parameter. The specific score ranking is shown (Fig. 5b).

As depicted in Fig. 5, the feature parameters of SWIM and SAR exhibit their respective advantages. The dominant features are mainly SWIM's slope spectral energy and backscattering coefficient under the nadir point, as well as SAR's normalized variance and incident angle, among others. This indicates that the feature parameters provided by SAR and SWIM both play a significant role in influencing the accuracy of wave and wind parameter inversion.

3.1.2 *Correlation analysis*

Prior to modeling with the dataset's feature parameters, feature selection is a critical step that significantly impacts the validity of the model's final results. During feature selection, an important factor to consider is whether there is multicollinearity among the features.

Collinearity can arise due to various reasons, including similar trends in two feature parameters, among others. Multicollinearity among features is common, necessitating its timely identification during the process of feature selection for modeling. Here, we employ the correlation coefficient test method to prevent the occurrence of feature collinearity.

The Pearson correlation coefficient is utilized to quantify the strength of linear correlation between two random variables. For two random variables, X and Y, the calculation formula is as follows:

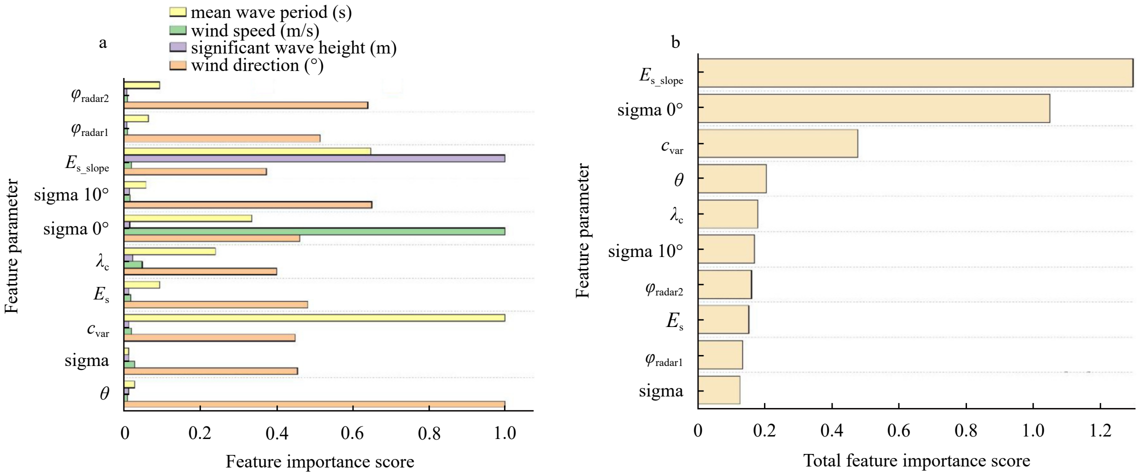

Fig. 5. Rank the importance of input feature parameters. a. The degree to which the feature influences each output parameter; b. the total influence of the feature on the output parameter.

$$r=\frac{\sum_{i=1}^{n}\left(X_i-\overline{X}\right)\left(Y_i-\overline{Y}\right)}{\sqrt{\sum_{i=1}^{n}\left(X_i-\overline{X}\right)^2}\sqrt{\sum_{i=1}^{n}\left(Y_i-\overline{Y}\right)^2}},\tag{14}$$

where n is the number of samples; X_i and Y_i are variables X and Y correspond to the observed value at point i; $\overline{X}$ is the average of X samples; $\overline{Y}$ is the average of Y samples. From this formula, the correlation coefficient values between features can be obtained, and the heat map of the correlation coefficient is shown (Fig. 6).

We can see the correlation between each feature intuitively through Fig. 6: absolute values of correlation coefficients between φ_{radar1} and φ_{radar2} is greater than 0.7, showing strong correlation. Finally, from the above two feature parameters, the parameter with a low importance score is removed successively: φ_{radar2}, while the other nine feature parameters are retained.

3.2 *Model establishment*

In this paper, the multi-output XGBoost algorithm is employed for model training, where the output variables are univariate. This approach allows for the establishment of an integrated inversion model for ocean wave and wind field parameters, designed to perform regression within a multi-output environment.

In this study, the utilization of collocated data between SAR and SWIM has been adopted. The coverage range for the SAR wave mode is 20 km × 20 km, while for SWIM, it is 70 km × 90 km. Therefore, when constructing the dataset, we did not perform segmentation on the SAR images. Each SAR mode image and its corresponding collocated SWIM box together constitute one set of data.

In this paper, a total of 26 740 data sets, comprising collocated SAR and SWIM data, were gathered over a span of four months, with one month representing each season, spanning the years 2019, 2020, and 2021. Initially, the data sets were randomly divided into training and test sets, maintaining a ratio of 7:3. This division resulted in 18 718 data sets designated for training the model, while the remaining 8 022 data sets were reserved for testing, allowing for the assessment of the accuracy of the trained sea wave and wind parameter predictions.

Additionally, for the sake of accuracy, the model's output results are compared with wave and wind field parameters derived from NDBC Buoys 46011 and 46054, particularly focusing on low and moderate wind speeds where buoys tend to provide more precise measurements. Furthermore, the study utilizes scatterometer and altimeter data that are matched with SAR and SWIM. These data enable a comprehensive comparison of the model's inversion results with parameters from various sources, including SWIM L2 products, SAR single loads, and a combined SAR and SWIM theoretical approach. The specific parameters under scrutiny are WS as provided by the scatterometer and SWH as provided by the altimeter.

4 Result analysis

4.1 *Comparison of model inversion results with wave and wind parameters provided by ECMWF*

To assess the model's performance, wave and wind parameters were retrieved from collocated SAR and SWIM data, and a detailed statistical analysis was conducted. In this section, the primary focus is on comparing the model's output parameters with the corresponding wave and wind parameters provided by ECMWF data. To gauge precision, standard error measures including RMSE, bias, and correlation coefficients (R) were employed as evaluation indices. The comparative results are presented (Table 2).

The comparison results presented in Table 2, between the

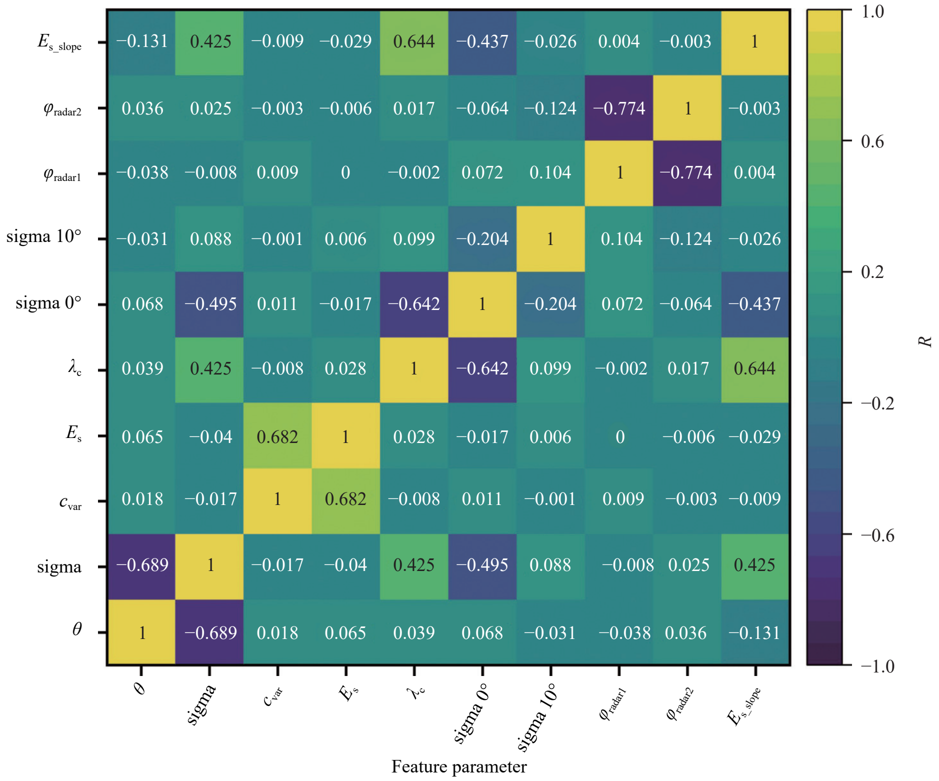

$E_{\text{s\_slope}}$	−0.131	0.425	−0.009	−0.029	0.644	−0.437	−0.026	0.004	−0.003	1
φ_{radar2}	0.036	0.025	−0.003	−0.006	0.017	−0.064	−0.124	−0.774	1	−0.003
φ_{radar1}	−0.038	−0.008	0.009	0	−0.002	0.072	0.104	1	−0.774	0.004
sigma 10°	−0.031	0.088	−0.001	0.006	0.099	−0.204	1	0.104	−0.124	−0.026
sigma 0°	0.068	−0.495	0.011	−0.017	−0.642	1	−0.204	0.072	−0.064	−0.437
λ_{c}	0.039	0.425	−0.008	0.028	1	−0.642	0.099	−0.002	0.017	0.644
E_{s}	0.065	−0.04	0.682	1	0.028	−0.017	0.006	0	−0.006	−0.029
c_{var}	0.018	−0.017	1	0.682	−0.008	0.011	−0.001	0.009	−0.003	−0.009
sigma	−0.689	1	−0.017	−0.04	0.425	−0.495	0.088	−0.008	0.025	0.425
θ	1	−0.689	0.018	0.065	0.039	0.068	−0.031	−0.038	0.036	−0.131
	θ	sigma	c_{var}	E_{s}	λ_{c}	sigma 0°	sigma 10°	φ_{radar1}	φ_{radar2}	$E_{\text{s\_slope}}$

Fig. 6. Heat map of the correlation coefficient between feature parameters.

Table 2. Comparison results of model output parameters with sea wave and wind parameters provided by ECMWF data

Parameter	RMSE	Bias	*R*
WD	27.446°	22.239°	0.899
WS	1.092 m/s	0.805 m/s	0.906
SWH	0.212 m	0.147 m	0.968
MWP	0.525 s	0.393 s	0.888

model's output parameters and the sea wave and wind parameters provided by ECMWF ERA5 data, indicate a close correspondence between the model's output values and the corresponding ERA5 parameters for WD, WS, SWH, and MWP. This alignment underscores the high parameter inversion accuracy achieved by the model established in this paper.

To provide a more intuitive analysis of the model's performance, a scatter diagram comparing the inversion model's output results with the ocean wave and wind parameters provided by ERA5 data is depicted (Fig. 7). The upper left corner of the figure displays the values of RMSE, bias, and *R*, which are used to evaluate the comparison between the model's inversion results and the sea wave and wind parameters provided by ECMWF ERA5 data.

4.2 *Comparison of model inversion results with wave and wind parameters provided by NDBC buoy data*

Buoys can provide relatively accurate wave and wind information. However, in hurricane sea conditions, buoys are prone to being overturned, leading to inaccurate observation data. Therefore, we excluded data with wind speeds exceeding 20 m/s.

Since collocated data of SAR and SWIM are primarily located in the ocean, while buoy data are mainly distributed in the nearshore area, only Buoy 46011 and Buoy 46054 can match SAR and SWIM simultaneously within the temporal and spatial scopes. A total of 28 sets of data during 2019 to 2021 have been collected.

Compared with the buoy data, the RMSE of the model's output parameters and the parameters provided by the buoy data are 27.698°, 1.315 m/s, 0.314 m, and 0.888 s, respectively (Table 3). The inversion accuracy of the model falls within the accepted error range, further demonstrating the effectiveness of the XGBoost-based inversion model for ocean wave and wind parameters established in this paper.

4.3 *Comparison of model inversion results with scatterometer and altimeter parameters*

Since the purpose of this paper is to realize the high-precision inversion of wave and wind parameters, the scatterometer and altimeter are recognized by researchers as satellites that can accurately obtain wave and wind parameters. Therefore, this section obtained 905 and 2 150 sets of matching SAR, SWIM, altimeter and scatterometer data, respectively.

Subsequently, the aforementioned dataset is employed as the

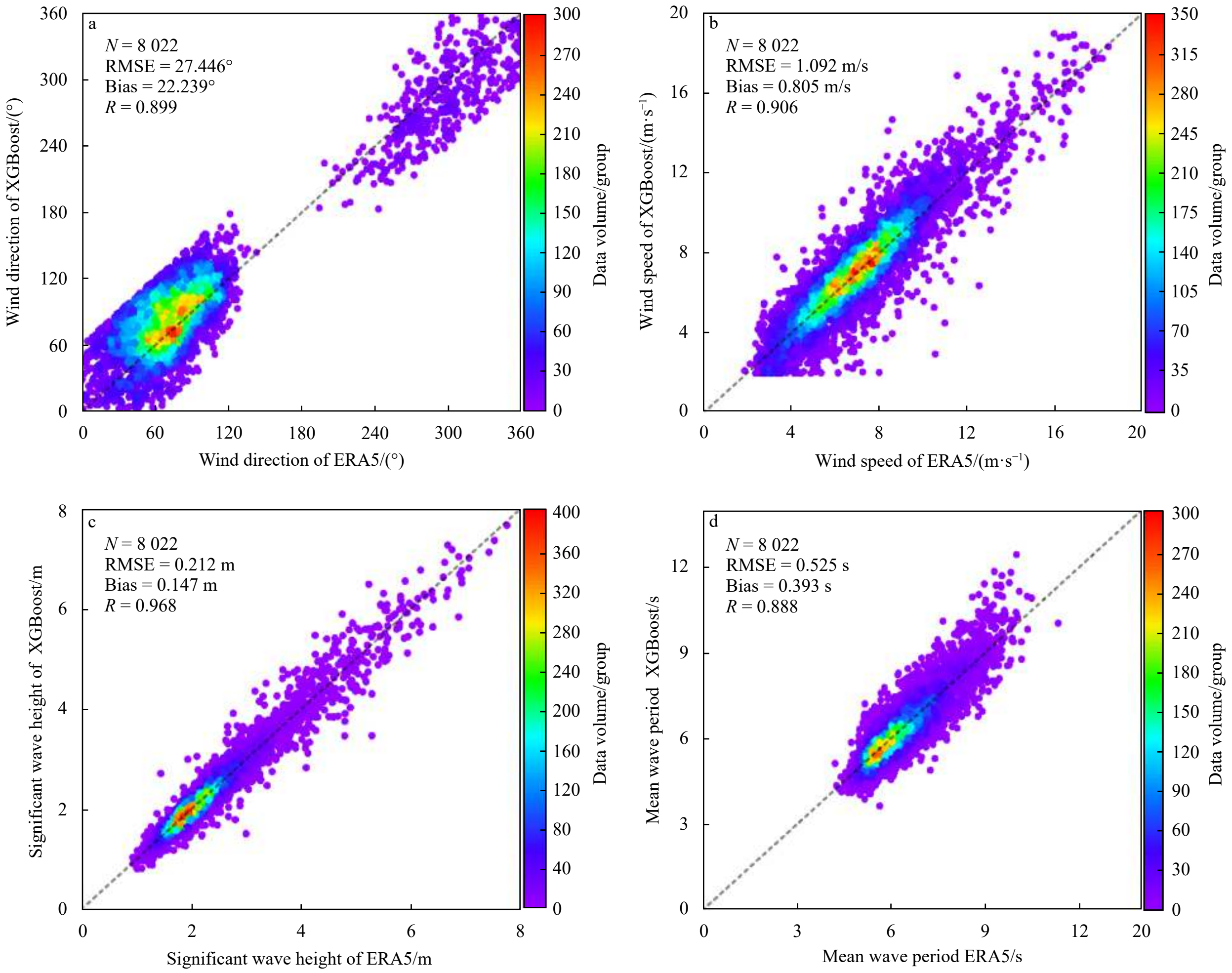

Fig. 7. Scatter plot of the output parameters of the model versus the wave and wind parameters provided by the ERA5 data. a. Wind direction, b. wind speed, c. significant wave height, d. mean wave period.

Table 3. The model outputs are compared with the wave and wind parameters provided by the NDBC buoy data

Parameter	RMSE	Bias	*R*
WD	27.698°	20.800°	0.870
WS	1.315 m/s	1.253 m/s	0.892
SWH	0.314 m	0.293 m	0.932
MWP	0.888 s	0.805 s	0.853

test set, and the model established in Section 3.2 is utilized to generate corresponding prediction results. Ultimately, the model's output of WS, SWH, and WD is compared with the data obtained from the altimeter and the scatterometer. The comparison results are presented (Table 4), revealing that the RMSE between the model's output parameters and the WS and SWH values obtained from the scatterometer and altimeter are 1.219 m/s and 0.326 m, respectively. These results indicate that the model's output closely aligns with the parameters provided by the scatterometer and altimeter, reaffirming the versatility of the model established in this paper.

The RMSE of the model's wind direction output compared to the wind direction from the scatterometer is 26.147°. In this paper, the anisotropy of the SWIM backscatter coefficient is primarily utilized for wind inversion. The degree of anisotropy increases with larger radar incidence angles. However, there are variations in the incidence angle ranges between the wave spectrometer, scatterometer, and the model output winds, leading to a certain gap between the wind values obtained from the model and those from the scatterometer.

Furthermore, it is essential to compare the results of joint inversion parameters obtained through the collocation of SAR and SWIM payloads with those from single payloads. Among the wave and wind information, SWH and WS are particularly important indicators (Huang et al., 2021). Therefore, we extracted information on SWH and WS from the SAR single payload inversion using the ocean wave parameter inversion method (MPI method) and wind field parameter inversion method (CMOD5.N method). Additionally, SWH and WS data were extracted from SWIM single payload using SWIM L2. Furthermore, we conducted a comparison between the inversion results and the model output parameters based on the theoretical Method of SAR/SWIM joint inversion of ocean wave and wind parameters (Method 1). In this comparison, the WS provided by the scatterometer and the SWH provided by the altimeter were used as the ground truth, and the results are presented (Table 5).

Table 4. The model output parameters are compared with the wave and wind parameters provided by scatterometer and altimeter data

Parameter	RMSE	Bias	*R*
WS	1.219 m/s	0.951 m/s	0.906
SWH	0.326 m	0.221 m	0.942
WD	26.147°	22.115°	0.893

The table above clearly demonstrates that the parameters obtained through the four methods closely align with the ground truth within an acceptable margin of error, allowing for the acquisition of relatively accurate parameters. In terms of WS comparison, the model inversion accuracy is on par with that of the SWIM single payload parameters, indicating similar wind speed inversion capabilities, with the model inversion slightly edging out in accuracy. Regarding SWH comparison, the model's output parameters exhibit higher accuracy. In summary, the model's inversion accuracy surpasses that of the other three methods.

This paper has categorized the test set data into four groups based on WS magnitude, as a result of employing varying data volumes for modeling under different sea conditions and the varying capabilities of the model for inverting wave and wind parameters. Subsequently, the four methods were compared in terms of WS and SWH, and the comparison results are depicted in (Figs 8a and b).

Analyzing the comparative statistical parameters presented in Fig. 8, we can observe the following:

(1) Comparing the SWH values obtained through the methods mentioned above, the model demonstrates higher accuracy when the WS is below 8 m/s. However, as the WS exceeds 8 m/s, the SWH accuracy diminishes with increasing WS. Nevertheless, in comparison to other methods, the model maintains a superior level of inversion accuracy. Furthermore, when the wind speed surpasses 12 m/s, there is a noticeable disparity between the

Table 5. The model output parameters are compared with those provided by scatterometer and altimeter

Method	RMSE		Bias	
	WS	SWH	WS	SWH
Model	1.219 m/s	0.326 m	0.951 m/s	0.221 m
SAR	1.548 m/s	0.434 m	1.136 m/s	0.342 m
SWIM	1.237 m/s	0.386 m	0.936 m/s	0.238 m
Method 1	1.358 m/s	0.413 m	1.025 m/s	0.329 m

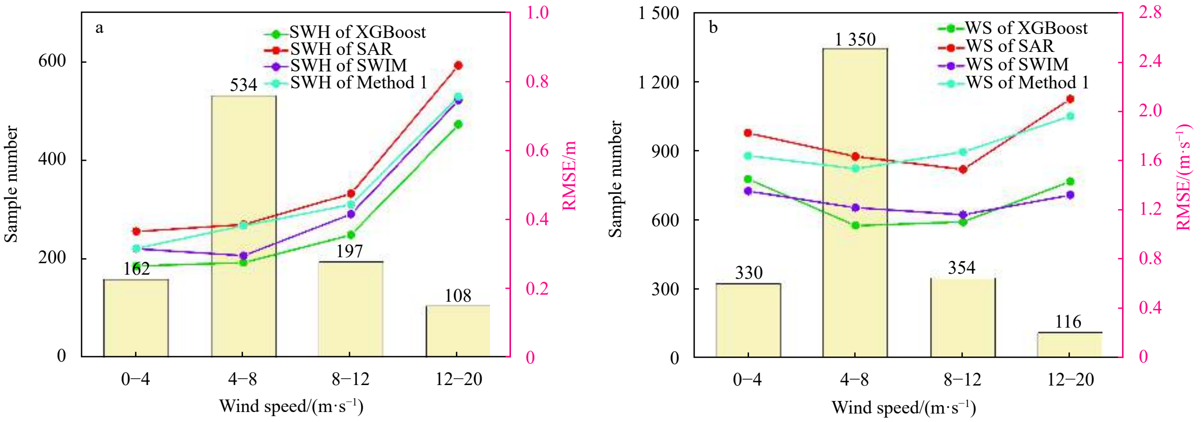

Fig. 8. Comparison of inversion results of different methods (the bar chart represents the sample number, while the line chart represents the values of RMSE). a. Significant wave height (SWH), b. wind speed (WS).

SWH obtained by the four methods and the SWH provided by the altimeter. This discrepancy may be attributed to the limited data points for high sea states, making it challenging to assess the accuracy of each method within this range. In summary, the model consistently exhibits higher SWH accuracy.

(2) Comparing the WS obtained through the methods mentioned above, as illustrated in Fig. 8b, the model's WS and the WS data provided by SWIM L2 products closely align with the WS from the scatterometer. Notably, when the WS falls between 4 m/s and 12 m/s, the model's WS output is more accurate. Furthermore, although the WS accuracy provided by SWIM L2 products is slightly higher when the WS is below 4 m/s or exceeds 12 m/s, the model's WS during these conditions still meets the acceptable WS error requirements. As indicated in Table 5, the overall inversion accuracy of the model surpasses that of SWIM.

(3) Based on a comprehensive analysis, it is evident that the inversion model utilizing SAR and SWIM data exhibits a significantly enhanced capability when compared to the other three methods.

In summary, the two types of sensors, SAR and wave spectrometer, mutually complement and enhance their capabilities. The method presented in this paper, based on the collocated data of SAR and wave spectrometer, achieves high-precision wave and wind parameter retrieval. This advancement holds great significance for enhancing microwave wave and wind field remote sensing capabilities and offers a novel approach for future wave and wind parameter detection efforts.

5 Conclusions

Using collocated data from Sentinel-1 SAR and SWIM, an empirical method for the joint inversion of wave and wind parameters is proposed in the paper. Initially, we extract feature parameters relevant to wind fields and sea waves from these two data sources. Next, we employ the XGBoost algorithm to rank the importance of these feature parameters, and we use correlation evaluation to mitigate the impact of feature collinearity to some extent. After adjusting the input parameters, inversion model is established. The accuracy of the sea wave and wind parameter inversion was assessed using ECMWF data as the ground truth, and statistical parameters like RMSE were utilized. Additionally, we compared the output parameters of the inversion model with those provided by NDBC buoys to further validate the accuracy of the retrieved wave and wind parameters. Furthermore, to confirm the precision of the model's retrieved parameters, we collected collocated data from SAR, SWIM, scatterometer, and altimeter sources, using the significant wave height from the altimeter and the wind parameters from the scatterometer as reference data. Then compared the results with those obtained from SAR single payload, SWIM single payload, and SAR/SWIM combined inversion. The outcomes are as follows:

(1) The parameters generated by the integrated inversion model for ocean wave and wind parameters closely align with those provided by ERA5 and buoy data. This suggests that the outcomes of the XGBoost feature importance analysis and correlation assessment are quite objective and rational, thus offering valuable insights for the selection of model feature parameters.

(2) Comparing the output parameters of the inversion model with the significant wave height and wind speed obtained by SAR single payload, SWIM single payload, and SAR and SWIM theory combined, using the wind speed and significant wave height provided by the scatterometer and altimeter as ground truth, reveals that the model's inversion accuracy is significantly superior to these methods.

Given the limited high sea state data available, the current inversion accuracy of wave and wind parameters during such conditions is relatively low. Consequently, the next phase of this research aims to assemble a more extensive dataset for high sea states and develop a suitable wave and wind field parameter inversion method using collocated SAR and spectrometer data. Additionally, the feasibility of integrating SAR and SWIM for retrieving wind wave parameters will be explored. The future direction involves the fusion of SAR and spectrometer data on a fixed grid, enabling the acquisition of high-precision wave and wind field information with enhanced spatial and temporal resolution worldwide. This endeavor holds significant implications for advancing the detection of marine meteorological parameters.

Acknowledgements

The authors acknowledge the National Data Buoy Center for buoy data, the ESA for Sentinel-1 satellite SAR Data, the CFOSAT data satellite service system for SWIM and SCAT data, and the European Center for Medium-range.

References

Alpers W R, Bruening C. 1986. On the relative importance of motion-related contributions to the SAR imaging mechanism of ocean surface waves. IEEE Transactions on Geoscience and Remote Sensing, GE-24(6): 873–885, doi: 10.1109/TGRS.1986.289702

Bruck M, Lehner S. 2013. Coastal wave field extraction using TerraSAR-X data. Journal of Applied Remote Sensing, 7(1): 073694, doi: 10.1117/1.JRS.7.073694

Bruck M, Lehner S. 2015. TerraSAR-X/TanDEM-X sea state measurements using the XWAVE algorithm. International Journal of Remote Sensing, 36(15): 3890–3912, doi: 10.1080/01431161.2015.1051630

Chen Tianqi, Guestrin C. 2016. XGBoost: a scalable tree boosting system. In: Proceedings of the 22nd ACM SIGKDD International Conference on Knowledge Discovery and Data Mining. San Francisco, California,USA: ACM,785–794

Han Qianqian, Hu Jijun, Song Shiyan, et al. 2013. Simulation on retrieval method of significant wave height from ocean wave spectrometer. Journal of Telemetry, Tracking and Command (in Chinese), 34(6): 7–13

Hasselmann K, Hasselmann S. 1991. On the nonlinear mapping of an ocean wave spectrum into a synthetic aperture radar image spectrum and its inversion. Journal of Geophysical Research: Oceans, 96(C6): 10713–10729, doi: 10.1029/91JC00302

Hauser D, Caudal G, Rijckenberg G J, et al. 1992. RESSAC: A new airborne FM/CW radar ocean wave spectrometer. IEEE Transactions on Geoscience and Remote Sensing, 30(5): 981–995, doi: 10.1109/36.175333

Hauser D, Soussi E, Thouvenot E, et al. 2001. SWIMSAT: a real-aperture radar to measure directional spectra of ocean waves from space—Main characteristics and performance simulation. Journal of Atmospheric and Oceanic Technology, 18(3): 421–437, doi: 10.1175/1520-0426(2001)018<0421:SARART>2.0.CO;2

He Yijun. 1999. A parametric method of retrieving ocean wave spectra from synthetic aperture radar images. Chinese Science Bulletin, 44(13): 1218–1224, doi: 10.1007/BF02885970

Hersbach H, Stoffelen A, de Haan S. 2007. An improved C-band scatterometer ocean geophysical model function: CMOD5. Journal of Geophysical Research: Oceans, 112(C3): C03006

Hersbach H. 2010. Comparison of C-band scatterometer CMOD5. N equivalent neutral winds with ECMWF. Journal of Atmospheric and Oceanic Technology, 27(4): 721–736, doi: 10.1175/2009JTECHO698.1

Huang Weimin, Liu Xinlong, Gill E W. 2017. An empirical mode decomposition method for sea surface wind measurements from X-band nautical radar data. IEEE Transactions on Geoscience and Remote Sensing, 55(11): 6218–6227, doi: 10.1109/TGRS.

2017.2723431

Huang Weimin, Yang Zhiding, Chen Xinwei. 2021. Wave height estimation from X-band nautical radar images using temporal convolutional network. IEEE Journal of Selected Topics in Applied Earth Observations and Remote Sensing, 14: 11395–11405, doi: 10.1109/JSTARS.2021.3124969

Jackson F C. 1987. The physical basis for estimating wave-energy spectra with the radar ocean-wave spectrometer. Johns Hopkins APL Technical Digest, 8: 70–73

Kerbaol V, Chapron B, El Fouhaily T, et al. 1996. Fetch and wind dependence of SAR azimuth cutoff and higher order statistics in a mistral wind case. In: Proceedings of 1996 International Geoscience and Remote Sensing Symposium. Lincoln, NE, USA: IEEE,621–624

Li Peng. 2019. The study on spaceborne spectrometer for sea surface wind field retrieval (in Chinese)[dissertation]. Wuhan: Huazhong University of Science and Technology

Li Xiaoming, Lehner S, Bruns T. 2011. Ocean wave integral parameter measurements using Envisat ASAR wave mode data. IEEE Transactions on Geoscience and Remote Sensing, 49(1): 155–174, doi: 10.1109/TGRS.2010.2052364

Li Xiaofeng, Pichel W G, He Mingxia. 2002. Observation of hurricane-generated ocean swell refraction at the Gulf Stream north wall with the radarsat-1 synthetic aperture radar. IEEE Transactions on Geoscience and Remote Sensing, 40(10): 2131–2142, doi: 10.1109/TGRS.2002.802474

Lin Wenming, Dong Xiaolong. 2011. Design and optimization of a Ku-band rotating, range-gated fanbeam scatterometer. International Journal of Remote Sensing, 32(8): 2151–2171, doi: 10.1080/01431161003674626

Liu Jiang, Xu Kangzhi, CAI Baigen, et al. 2021. XGBoost-based fault prediction method for on-board train control equipment. Journal of Beijing Jiaotong University (in Chinese), 45(4): 95–106

Mastenbroek C, De Valk C F. 2000. A semiparametric algorithm to retrieve ocean wave spectra from synthetic aperture radar. Journal of Geophysical Research: Oceans, 105(C2): 3497–3516, doi: 10.1029/1999JC900282

Pleskachevsky A, Jacobsen S, Tings B, et al. 2019. Estimation of sea state from Sentinel-1 Synthetic aperture radar imagery for maritime situation awareness. International Journal of Remote Sensing, 40(11): 4104–4142, doi: 10.1080/01431161.2018.1558377

Pleskachevsky A L, Rosenthal W, Lehner S. 2016. Meteo-marine parameters for highly variable environment in coastal regions from satellite radar images. ISPRS Journal of Photogrammetry and Remote Sensing, 119: 464–484, doi: 10.1016/j.isprsjprs.2016.02.001

Pleskachevsky A, Tings B, Wiehle S, et al. 2022. Multiparametric sea state fields from synthetic aperture radar for maritime situational awareness. Remote Sensing of Environment, 280: 113200, doi: 10.1016/j.rse.2022.113200

Quilfen Y, Chapron B, Elfouhaily T, et al. 1998. Observation of tropical cyclones by high - resolution scatterometry. Journal of Geophysical Research: Oceans, 103(C4): 7767–7786, doi: 10.1029/97JC01911

Ren Lin, Yang J, Xu Y, et al. 2021. Ocean surface wind speed dependence and retrieval from off - nadir CFOSAT SWIM data. Earth and Space Science, 8(6): e2020EA001505, doi: 10.1029/2020EA001505

Ren Lin, Yang Jingsong, Zheng Gang, et al. 2016. A joint method to retrieve directional ocean wave spectra from SAR and wave spectrometer data. Chinese Journal of Oceanology and Limnology, 34(4): 847–858, doi: 10.1007/s00343-015-5043-4

Rikka S, Pleskachevsky A, Jacobsen S, et al. 2018. Meteo-marine parameters from Sentinel-1 SAR imagery: towards near real-time services for the Baltic sea. Remote Sensing, 10(5): 757, doi: 10.3390/rs10050757

Schulz-Stellenfleth J, Konig T, Lehner S. 2006. An empirical approach for the retrieval of ocean wave parameters from synthetic aperture radar data. In: Proceedings of 2006 IEEE International Symposium on Geoscience and Remote Sensing. Denver, CO, USA: IEEE

Schulz-Stellenfleth J, Lehner S, Hoja D. 2005. A parametric scheme for the retrieval of two-dimensional ocean wave spectra from synthetic aperture radar look cross spectra. Journal of Geophysical Research: Oceans, 110(C5): C05004

Shao Weizeng, Wang Jing, Li Xiaofeng, et al. 2017. An empirical algorithm for wave retrieval from Co-polarization X-Band SAR imagery. Remote Sensing, 9(7): 711, doi: 10.3390/rs9070711

Spencer M W, Wu C, Long D G. 1997. Tradeoffs in the design of a spaceborne scanning pencil beam scatterometer: application to SeaWinds. IEEE Transactions on Geoscience and Remote Sensing, 35(1): 115–126, doi: 10.1109/36.551940

Stoffelen A, Anderson D. 1997. Scatterometer data interpretation: Estimation and validation of the transfer function CMOD4. Journal of Geophysical Research: Oceans, 102(C3): 5767–5780, doi: 10.1029/96JC02860

Stopa J E, Mouche A. 2017. Significant wave heights from Sentinel-1 SAR: validation and applications. Journal of Geophysical Research: Oceans, 122(3): 1827–1848, doi: 10.1002/2016JC012364

Wan Yong, Zhang Xiaona, Fan Chenqing, et al. 2022. A joint method for wave and wind field parameter inversion combining SAR with wave spectrometer data. Remote Sensing, 14(15): 3601, doi: 10.3390/rs14153601

Wang Xiaochen. 2016. Research on airborne spectrometer wave spectrum inversion method (in Chinese)[dissertation]. Qingdao: China University of Petroleum (East China)

Wang He, Yang Jingsong, Lin Mingsen, et al. 2022. Quad-polarimetric SAR sea state retrieval algorithm from Chinese Gaofen-3 wave mode imagettes via deep learning. Remote Sensing of Environment, 273: 112969, doi: 10.1016/j.rse.2022.112969

Zou Bin, Lin Mingsen, Shi Lijian, et al. 2018. Application of remote sensing technology in ocean disaster. City and Disaster Reduction (in Chinese), (6): 61–65